Carbon nitride boosts the CO_2 methanation activity of Ni/CeO_2

Yingrui Zhao [a], Plaifa Hongmanorom [a], Feilong Yang [a], Sandra Casale [b], Capucine Sassoye [c], Ales Styskalik [d], Damien P. Debecker*, [a]

[a] Université catholique de Louvain (UCLouvain), Institute of Condensed Matter and Nanosciences (IMCN), Place Louis Pasteur, 1, box L4.01.09, 1348 Louvain-La-Neuve, Belgium.

[b] Sorbonne Université, Laboratoire de Réactivité de Surface, CNRS UMR 7197, 4 Place Jussieu, 75005, Paris, France.

[c] Sorbonne Université, Chimie de la Matière Condensée de Paris, UMR 7574, 4 Place Jussieu, 75005 Paris, France.

[d] Department of Chemistry, Masaryk University, Kotlarska 2, CZ-61137, Brno, Czech Republic.

* Corresponding autor:
E-mail: damien.debecker@uclouvain.be
Tel: +32 10473648
ORCID: 0000-0001-6500-2996

ABSTRACT

Selective CO_2 methanation using green H_2 offers a promising approach for tackling both energy and environmental challenges. Herein, a Ni/CeO_2 catalyst was synthesized using a one-pot method in the presence of sacrificial C_3N_4 and evaluated for CO_2 methanation. The catalyst exhibited a high CO_2 conversion of 82.6% and a CH_4 production rate of up to 178 mmol g_{cat}^{-1} h^{-1}, with high CH_4 selectivity (99.4%) at a remarkably low temperature of 250 °C. Surface characterization techniques, including Raman spectroscopy, XPS, ^{31}P-MAS-NMR of adsorbed trimethylphosphine, and CO_2-TPD, demonstrate that the addition of C_3N_4 significantly enhanced the concentration of surface oxygen vacancies and medium-strength basic sites. In situ DRIFTS analysis indicated that CO_2 methanation over Ni/CeO_2 proceeded via the RWGS+CO hydrogenation and formate pathways, with the former being predominant at low temperatures. The exceptional low-temperature methanation performance of this new catalyst is attributed to the increased density of oxygen vacancies and medium-strength basic sites.

1. INTRODUCTION

CO_2 methanation ($CO_2 + 4H_2 \rightarrow CH_4 + 2H_2O$, ΔH_{298K} = -165 kJ mol^{-1}), the so-called Sabatier reaction, has attracted extensive attention for several decades owing to its potential for CO_2 recycling and optimizing energy structures.[1,2] Given the exothermic nature of the reaction, low reaction temperature is beneficial to the effectiveness of this process.[3] On the contrary, high reaction temperature is required due to the chemical inertness and thermodynamic stability of the CO_2 molecule.[4] Among the numerous kinds of catalysts for CO_2 methanation, Ni-based catalysts are the most studied due to their high catalytic performance (above 300 °C) and attractive cost-effectiveness.[5,6] However, there is still a great challenge to achieve a superior low temperature methanation activity (especially below 250 °C) for the Ni-based catalysts.

The CO_2 methanation mechanism can be categorized into formate pathway and RWGS+CO hydrogenation pathway.[7–10] Instead of mutually independent, those two pathways could occur in parallel.[11,12] Formate pathway involves the stepwise hydrogenation of adsorbed CO_2 species into CH_4 with the formate from the hydrogenation of monodentate carbonate as an important intermediate. In this pathway, tailoring the catalyst basicity is thought to be a key strategy for tuning the CO_2 adsorption behavior. Monodentate carbonate originates from the adsorption of CO_2 on medium basic sites, and medium basicity is widely accepted as optimal for CO_2 methanation.[13] Pan et al. combined CO_2-TPD and in-situ FTIR analyses and proposed that intermediate species formed on the medium basic sites of $Ni/Ce_{0.5}Zr_{0.5}O_2$ could be converted to methane more quickly than those on weak basic sites.[14] Additionally, they reported that the strong basic sites of Ni/Al_2O_3 could hinder further hydrogenation of carbonate intermediates.

RWGS+CO hydrogenation pathway involves the dissociation of CO_2 to CO, followed by the subsequent hydrogenation of CO to CH_4. According to the literature, enhancing CO_2 activation represents a promising approach to improving catalytic performance.[15,16] Different strategies have been developed in an attempt to promote this

process. One key strategy is to select proper support. Among the numerous candidates, CeO_2 is an interesting support due to the abundant surface oxygen vacancies and redox properties.[17–21] Another crucial step is to choose a preparation method. Rui et al. prepared a Ni/CeO_2 catalyst by a low-temperature plasma decomposition method, which led to an interfacial structure where Ni atoms bind with O atoms from ceria and caused a strong metal-support interaction.[22] As a result, the plasma prepared Ni/CeO_2 catalysts with small particle size and abundant metallic Ni as active sites for splitting H_2 showed balanced active sites for H_2 splitting and CO_2 activation, and thus high catalytic activity at low temperature. Ye et al. prepared a Ni/CeO_2 catalyst by citrate sol-gel method.[23] The synergy of efficient dissociation of H_2 by small nickel nanoparticles and the strong adsorption and activation of CO_2 by CeO_2 support resulted in the high activity of the prepared catalyst. Clearly, the preparation method has a strong influence on the catalyst properties and related performance.

In this study, a high-performance Ni/CeO_2 catalyst (denoted Ni/CeO_2-CN-OP) is prepared by one-pot method assisted with carbon nitride (C_3N_4). While C_3N_4 is known as a good catalyst support for electro- and photocatalytic CO_2 reduction processes,[24–26] it is here simply used as an additive during the catalyst preparation. Despite being removed by calcination at the end of the catalyst preparation, C_3N_4 is shown to significantly modify the catalyst properties. The exceptional methanation activity of Ni/CeO_2-CN-OP is attributed to an increased concentration of oxygen vacancies, as well as a higher density of medium basic sites on the catalyst surface. Furthermore, the CO_2 methanation mechanism is investigated by in-situ diffuse reflectance infrared Fourier transform spectroscopy (DRIFTS), showing that the activation of CO_2 and the conversion of monodentate carbonate species are notably enhanced.

2. MATERIALS AND METHODS

Catalyst Synthesis. Synthesis of carbon nitride. C_3N_4 was prepared by heating dicyandiamide (about 10 g) in a crucible with a cover to 550 °C for 2 h at a ramp rate of 5 °C/min in a muffle furnace.[27] After being cooled to room temperature naturally, the obtained yellow product was ground into powder and designated as CN. The XRD pattern shown in Figure S7 confirms successful synthesis of C_3N_4 configuration.

Synthesis of CeO_2 support. CeO_2 support was obtained by calcining the $Ce(NO_3)_3 \cdot 6H_2O$ in a covered crucible to 550 °C for 4 h with a ramp rate of 5 °C/min in a muffle furnace.

Synthesis of CeO_2(CN) support. 2.2706 g of $Ce(NO_3)_3 \cdot 6H_2O$ was dissolved in 40 mL water. After stirring for 1 h, 2 g C_3N_4 powder was added into the solution and continuously stirred at room temperature for 4 h. The mixture was evaporated in the water bath at 70 °C under vigorous stirring and then further dried at 70 °C overnight. The obtained solids were calcined in a crucible with a cover at 550 °C for 4 h with a ramp rate of 5 °C/min in a muffle furnace.

Synthesis of Ni/CeO_2-CN-OP catalyst. Ni/CeO_2-CN-OP catalyst was prepared in one-pot method. Typically, 2.2706 g of $Ce(NO_3)_3 \cdot 6H_2O$ and 1.1014 g $Ni(NO_3)_2 \cdot 6H_2O$ were dissolved in 40 mL water. After stirring for 1 h, 2 g C_3N_4 powder was added into the solution and continuously stirred at room temperature for 4 h. The mixture was evaporated in the water bath at 70 °C under vigorous stirring and then further dried at 70 °C overnight. The obtained solids were calcined in a crucible with a cover at 550 °C for 4 h with a ramp rate of 5 °C/min in a muffle furnace. Finally, the samples were reduced under a pure H_2 flow (20 mL/min) at 350 °C for 2 h. The sample preparation protocol is illustrated in Scheme 1. Ni/CeO_2-OP catalyst was prepared in the same way as Ni/CeO_2-CN-OP without adding the CN in the preparation process.

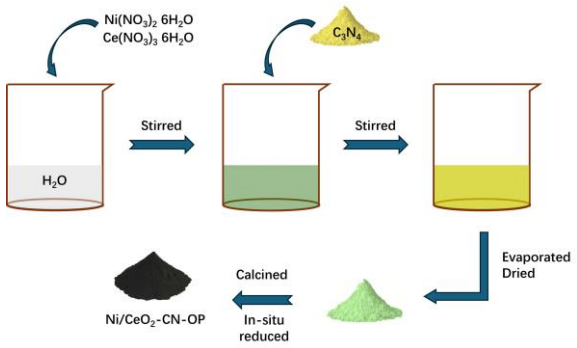

Scheme 1. Sample preparation protocol.

For comparison, Ni/CeO_2-IM and Ni/CeO_2(CN)-IM were synthesized with conventional impregnation method. The CeO_2 or CeO_2(CN) support was impregnated into the aqueous solution of $Ni(NO_3)_2 \cdot 6H_2O$. After stirring for 1 h, the mixture was evaporated in the water bath at 70 °C under vigorous stirring and then further dried at 70 °C overnight. The obtained solids were calcined and reduced in the same method used for treating Ni/CeO_2-CN-OP. The final obtained catalysts are denoted Ni/CeO_2-IM and Ni/CeO_2(CN)-IM, respectively.

Catalyst Characterization. The morphologies, textural properties, crystal structure, surface properties of the bare CeO_2 supports and Ni/CeO_2 catalysts were characterized by transmission electron microscopy (TEM), N_2 adsorption-desorption, X-ray diffraction (XRD), H_2 chemisorption, inductively coupled plasma-atomic emission spectroscopy (ICP-AES), H_2 temperature-programmed reduction (H_2-TPR), CO_2 temperature-programmed desorption (CO_2-TPD), Raman spectroscopy, X-ray photoelectron spectroscopy (XPS), solid state nuclear magnetic resonance (NMR). The catalytic behavior of active sites and the CO_2 methanation mechanism over Ni/CeO_2 catalysts were explored by in situ DRIFTS experiments. The details of characterizations are listed in the Supporting Information (SI).

Catalyst Testing. The catalytic performance testing was performed using an in-house reaction setup (for details see Figure S1). Typically, 50 mg of catalyst was in situ

reduced at 350 °C for 2 h under pure H_2 flow (20 mL/min). After the catalyst bed was cooled to 200 °C under He flow, a 30 mL/min feed gas consisting of 13.3% CO_2/53.2% H_2/He (CO_2 = 4 mL/min, H_2 = 16 mL/min, He = 10 mL/min) was introduced into the reactor, corresponding to a gas hourly space velocity (GHSV) of 36,000 mL g^{-1} h^{-1}. The test was carried out in the temperature range of 200−325 °C at a temperature interval of 25 °C. The gas exiting the reactor was analyzed on a gas chromatograph (Varian CP3800), equipped with Hayesep Q, Molsieve 5A, and CP-Sil-5CB columns. The separated gases were analyzed with a flame ionization detector (CH_4) and a thermal conductivity detector (CO and CO_2). All transfer lines were maintained at 125 °C to avoid water condensation. Conversion (X_{CO2}) and selectivity (S_{CH4}) were calculated according to the following equations (Eq. (1) and (2), respectively):

$$X_{CO2} = \frac{F_{CO_2,in} - F_{CO_2,out}}{F_{CO_2,in}} \quad (1)$$

$$S_{CH4} = \frac{F_{CH_4,out}}{F_{CO_2,in} - F_{CO_2,out}} \quad (2)$$

where F is the molar flow rate. The turnover frequency (TOF) was calculated by the following equation (Eq. (3)):

$$\text{TOF } (s^{-1}) = \frac{X_{CO_2} \times F_{CO_2,in}}{\text{mole of surface Ni atoms}} \quad (3)$$

3. RESULTS AND DISCUSSION

3.1. Structure and Morphology. Textural properties of the supports and reduced catalysts were measured by N_2 adsorption, as shown in Figure S2. The detailed textural parameters were listed in Table S1. The profile of CeO_2 (Figure S2a) displays a type IV isotherm, indicating the existence of mesoporous structure.[28] The apparent H2 type hysteresis loop is associated with capillary condensation taking place in the particles with neck bottle-shaped pores.[29] The surface area, pore volume, and average pore diameter of CeO_2 are 68 m^2 g^{-1}, 0.22 cm^3 g^{-1}, and 10.9 nm, respectively. As C_3N_4 was added during the preparation of CeO_2(CN), the type IV isotherm with H2 hysteresis loop remains basically unchanged (Figure S2a). Compared with CeO_2, the surface area,

pore volume, and average pore diameter of CeO_2(CN) increased to 79 m^2 g^{-1}, 0.29 cm^3 g^{-1}, and 13.2 nm, respectively, which is due to removal of C_3N_4 during the calcination process. The impregnation of Ni decreases these three parameters of both the Ni/CeO_2-IM and Ni/CeO_2(CN)-IM catalysts compared with the corresponding supports. For the catalysts prepared by one-pot method, the profile of Ni/CeO_2-OP also displays the type IV isotherms with H2 type hysteresis loop (Figure S2b). Differently, mesoporous Ni/CeO_2-CN-OP catalyst shows H3 type hysteresis loop, characteristic of plate-type particles with slit-shaped pores.[30] The average pore diameter of Ni/CeO_2-OP and Ni/CeO_2-CN-OP is in the same range of 8.5-8.9 nm. Ni/CeO_2-CN-OP exhibits a smaller BET surface area (50 m^2 g^{-1}) and total pore volume (0.11 cm^3 g^{-1}) than Ni/CeO_2-OP (89 m^2 g^{-1}, 0.23 cm^3 g^{-1}).

XRD measurement was performed to identify the crystal structure of the supports and reduced catalysts. For all bare CeO_2 support (Figure S3a) and Ni/CeO_2 catalysts (Figure S3b), the main diffraction peaks at 28.6, 33.1, 47.5, 56.4, 59.1, 69.4, 76.7 and 79.1° can be attributed to the (111), (200), (220), (311), (222), (400), (331) and (420) planes of CeO_2 in fluorite structure (PDF 34-0394). Moreover, the diffraction peaks at 44.5 and 51.8° originate from the (111) and (200) planes in the Ni^0 cubic structure (PDF 04-0850).[31] The morphologies of Ni/CeO_2 were investigated using (HR)TEM. As shown in Figure 1a-1d, Ni/CeO_2-CN-OP exhibits smaller particles compared with Ni/CeO_2-OP, Ni/CeO_2-IM and Ni/CeO_2-CN-IM. However, the small difference in the contrast between Ni and CeO_2 makes it difficult to discern them.[32,33] EDX analysis (inset Figure 1a-1d) confirmed the presence of nickel. Furthermore, much more serious agglomeration can be observed over Ni/CeO_2-OP and Ni/CeO_2-IM compared with Ni/CeO_2-CN-OP. While only qualitative, this observation is consistent with the sharper Ni diffraction peaks observed for these samples. In contrast, the broader Ni peaks in Ni/CeO_2-CN-OP indicate smaller, more highly dispersed Ni nanoparticles, reflecting better stabilization by the g-C_3N_4-assisted synthesis. Higher Ni dispersion (9.4%) in Ni/CeO_2-CN-OP compared with that in Ni/CeO_2-OP (7.1%), Ni/CeO_2-IM (5.5%), and

Ni/CeO_2(CN)-IM (8.5%) is also confirmed by H_2 chemisorption measurement, as presented in Table S1. The average metal particle size can be further estimated from dispersion, and the higher dispersion of Ni/CeO_2-CN-OP reveals the smaller particle size on its surface. The lattice fringes of the metal nanoparticles are also visible in HRTEM images. In Figure 1e-1h, the clear lattice fringe distances are 0.19, 0.27 and 0.31 nm, corresponding to the CeO_2 (220), CeO_2 (200) and CeO_2 (111) planes, respectively. The first two suggest the presence of CeO_2 (110) and (100) planes, respectively.[34]

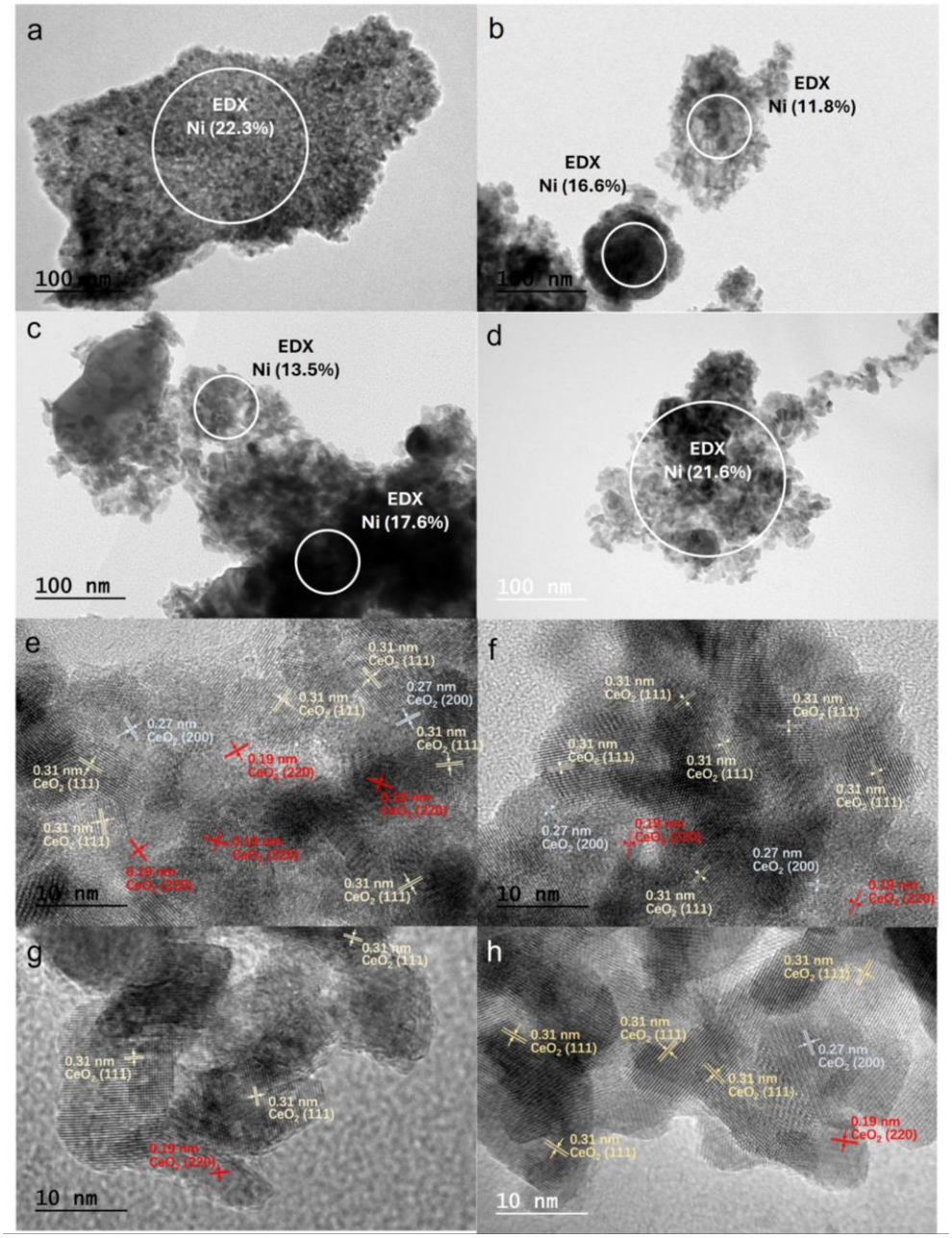

Figure 1. TEM images of (a) Ni/CeO_2-CN-OP, (b) Ni/CeO_2-OP, (c) Ni/CeO_2-IM, and (d) Ni/CeO_2-CN-IM. HRTEM images of (e) Ni/CeO_2-CN-OP, (f) Ni/CeO_2-OP, (g) Ni/CeO_2-IM, and (h) Ni/CeO_2-CN-IM.

3.2. Reducibility and Basicity. The reducibility of the Ni/CeO_2 catalysts and the corresponding support was investigated using H_2-TPR measurements, as shown in Figure 2a and Figure S4. For CeO_2 supports (Figure S4), small reduction peaks at 400-600 °C and 700-900 °C can be attributed to the reduction of surface capping oxygen and bulk lattice oxygen of CeO_2, respectively.[35] For all the Ni/CeO_2 catalysts, two major H_2 consumption peaks, labeled as β and δ, can be distinguished (Figure 2a). The β peaks centered in the temperature range of 310-370 °C can be attributed to reduction of NiO species moderately (β_1, 310-330 °C) and strongly (β_2, 360-410 °C) interacting with CeO_2.[13] Obviously, the proportion of NiO strongly interacting with CeO_2 is significantly higher in catalysts synthesized via the one-pot method compared to those prepared by the impregnation method. Furthermore, the incorporation of C_3N_4 further enhances this interaction. These findings indicate that the one-pot synthesis approach, combined with C_3N_4 addition, effectively strengthens the metal-support interaction. The δ peak located at around 750 °C shows the reduction of crystalline CeO_2 from Ce^{4+} to Ce^{3+}. In addition to these two major peaks (β and δ), for the Ni/CeO_2(CN)-IM, Ni/CeO_2-OP and Ni/CeO_2-CN-OP catalysts, a new reduction peak (labeled as α) at lower temperature (190-230 °C) is detected. According to the literature, this peak is ascribed to the reduction of adsorbed oxygen species, which is from the Ni-O-Ce interfacial sites and can be easily removed by hydrogen.[22,23] There is no α reduction peak for Ni/CeO_2-IM and Ni/CeO_2-CN-OP has larger α peak than Ni/CeO_2-OP and Ni/CeO_2(CN)-IM, which indicate that C_3N_4 addition and one-pot preparation method could facilitate the formation of Ni-O-Ce solid solution. The Ni/CeO_2-CN-OP catalyst also shows an extra peak at 440 °C (labeled as γ), which is related to the surface reduction of CeO_2 by spillover hydrogen at the Ni-CeO_2 interface.[36]

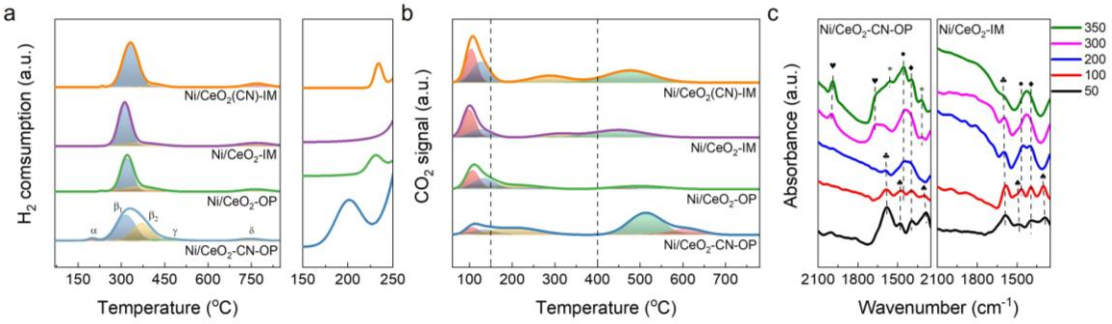

Figure 2. (a) H_2-TPR profiles of the Ni/CeO_2 catalysts; (b) CO_2-TPD spectra of Ni/CeO_2 catalyst; (c) in-situ CO_2 desorption DRIFTS of the Ni/CeO_2-CN-OP and Ni/CeO_2-IM catalyst. Symbol definition: bicarbonate (♠), monodentate carbonate (♣), bidentate carbonate (◆), polydentate carbonate (•), monodentate formate (∗), carbonyl (♥).

CO_2-TPD measurement was performed to evaluate the basicity of the Ni/CeO_2 catalysts. The CO_2 desorption curve (Figure 2b) is fitted and divided into three temperature regions based on basicity strength including 50-150 °C, 150-400 °C and 400-700 °C, which are ascribed to weak, medium, and strong basic site, separately.[5] A series of works indicated that increasing the amount of medium basic site could promote the methanation performance, while the strong basic sites did not play a positive role in enhancing methanation activity due to the suppression of further hydrogenation.[14,37,38] For comparison, Table S2 presents the amount of desorbed CO_2. It can be seen that the Ni/CeO_2-CN-OP has the lowest amount of weak basic site compared with the other three catalysts. On the contrary, medium and strong basic sites predominate over Ni/CeO_2-CN-OP, and the amount of medium and strong basic sites are higher than the other three catalysts.

The adsorbed CO_2 species were further investigated using the in-situ DRIFTS characterization. As shown in Figure 2b, after being saturated by CO_2 and then flushed under He atmosphere at 50 °C for 30 min, the spectrum of Ni/CeO_2-CN-OP and Ni/CeO_2-IM both displays clear signature of bicarbonate (1482, 1295 cm^{-1}), monodentate carbonate (1582 cm^{-1}), and bidentate carbonate (1398 cm^{-1}).[39–41] For Ni/CeO_2-CN-OP and Ni/CeO_2-IM, the peaks for the bicarbonate species decrease progressively and could be removed totally below 200 °C. For the monodentate

carbonate species, increasing the temperature also leads to a gradual decrease of peak intensity on Ni/CeO_2-CN-OP and Ni/CeO_2-IM. When the temperature increases to 300 °C, the peak for monodentate carbonate on Ni/CeO_2-CN-OP disappears completely. However, there is still a small shoulder peak for monodentate carbonate on Ni/CeO_2-IM until the temperature increases to 350 °C. The intensity of bidentate carbonate peak remains almost unchanged below 350 °C. Meanwhile, the formation of polydentate carbonate species (1454 cm^{-1})[42] occurs above 100 °C on Ni/CeO_2-CN-OP and Ni/CeO_2-IM, and extra peaks attributed to carbonyl and monodentate formate species are formed on Ni/CeO_2-CN-OP.

Based on the results of CO_2-TPD and in-situ DRIFTS, the amount and nature of the adsorbed CO_2 species are identified. Specifically, CO_2 can adsorb on weak basic site and form bicarbonate, which could be removed from the catalyst surface below 200 °C. Meanwhile, CO_2 adsorption on medium basic sites results in the formation of monodentate carbonates, the amount of which decreases in the following order: Ni/CeO_2-CN-OP > Ni/CeO_2(CN)-IM > Ni/CeO_2-OP > Ni/CeO_2-IM as presented in Table S2.

3.3. Oxygen Vacancies. Oxygen vacancies are critical defects in cerium-based catalysts for CO_2 methanation, as they play a key role in facilitating CO_2 activation. The formation and concentration of oxygen vacancies were evinced and estimated by Raman spectra and XPS. The observed Raman features of the CeO_2 supports (Figure S5) at 462 and 598 cm^{-1} are assigned to the vibration model of octahedral local symmetry from the CeO_2 lattice (F_{2g}) and defect-induced mode (D), respectively.[42] The ratio of the intensity for the D band and F_{2g} band is calculated to evaluate oxygen vacancy concentration. The ratio increases from 0.035 of CeO_2 to 0.045 of CeO_2(CN), which means that the addition of C_3N_4 would increase the amount of oxygen vacancies. The Raman features of the Ni/CeO_2 samples are displayed in Figure 3a. After the loading of Ni and reduction, a significant increase in the I_D/I_{F2g} value occurs (Figure 3b) as a result of Ni incorporation into CeO_2 lattice. The I_D/I_{F2g} value of Ni/CeO_2-CN-OP

(~0.59) is much higher than that of Ni/CeO_2-OP (~0.39), Ni/CeO_2-IM (~0.35) and Ni/CeO_2(CN)-IM (0.43), demonstrating more oxygen vacancies generated on Ni/CeO_2-CN-OP. Furthermore, an evidently lower Raman shift of F_{2g} band is observed for Ni/CeO_2-CN-OP, Ni/CeO_2-OP and Ni/CeO_2(CN)-IM. This shift indicates the lower symmetry of Ce–O bond in Ni/CeO_2-CN-OP, Ni/CeO_2-OP and Ni/CeO_2(CN)-IM, which can be explained by the formation of $Ni_xCe_{1-x}O_{2-\delta}$ solid solution in accordance with the H_2-TPR results.[43,44]

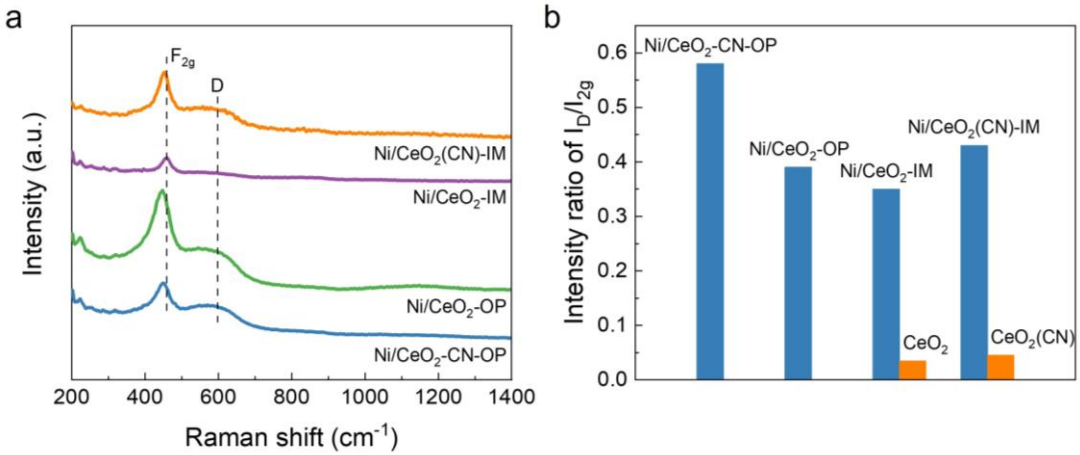

Figure 3. (a) Raman spectra and (b) relative intensity of I_D/I_{F2g} of the Ni/CeO_2 catalysts.

The information on surface elemental composition and the chemical state over the Ni/CeO_2 catalysts were also determined by XPS analysis. As shown in the Ni $2p_{3/2}$ spectra (Figure 4a), coexistence of Ni^0 (at 852.5 eV) and Ni^{2+} (at 855.2 eV and satellite at 860.6 eV) can be found for all catalysts.[38] The existence of Ni^{2+} is attributed to the formation of Ni-O-Ce solid solution mentioned above and the quick oxidation of active Ni in air.[23] The difference of surface Ni^0 percentage over these catalysts is small as displayed in Table S3. In the XPS spectra of O 1s (Figure 4b), two deconvoluted peaks at 529.3 eV and 531.3 eV can be assigned to lattice oxygen (O_L) and surface-adsorbed oxygen species (O_{ads}), including surface hydroxyl (OH) and carbonate (CO_3^{2-}). The presence of CO_3^{2-} is also evident from the peak at 288.7 eV in the C 1s spectra (Figure 4c).[10,45] The ratio of $O_{ads}/(O_{ads} + O_L)$, presented in Table S3, follows the order: Ni/CeO_2-CN-OP > Ni/CeO_2(CN)-IM > Ni/CeO_2-OP > Ni/CeO_2-IM. In this case, the

concentration of surface-adsorbed oxygen species may indirectly reflect the oxygen vacancy concentration, as gas molecules tend to adsorb preferentially onto oxygen vacancies.[46] Therefore, Ni/CeO_2-CN-OP has higher amount of oxygen vacancy on its surface due to its highest ratio of $O_{ads}/(O_{ads} + O_L)$, which aligns well with the oxygen vacancy concentration derives from Raman results. The Ce 3d spectra is shown in Figure 4d. The pairs of spin-orbit coupling ($3d_{5/2}$ and $3d_{3/2}$) are labeled as u and v, respectively. The peaks at 916.2 eV (u‴), 906.8 eV (u″), 900.5 eV (u), 897.7 eV (v‴), 888.4 eV (v″), and 882.1 eV (v‴) correspond to surface Ce^{4+} species, and the remaining four peaks at 902.3 eV (u′), 898.7 eV (u_0), 884.3 eV (v′), and 880.7 eV (v_0) are assigned to surface Ce^{3+} species.[47] According to the electrostatic balance mechanism, the ratio of $Ce^{3+}/(Ce^{4+} + Ce^{3+})$ could also reflect the content of oxygen vacancies. However, the difference in the ratio of $Ce^{3+}/(Ce^{4+} + Ce^{3+})$ between those four catalysts (Table S3) is smaller than that in the ratio of $O_{ads}/(O_{ads} + O_L)$. This discrepancy may be explained by the fact that the oxygen vacancy is more abundant on the surface because oxygen vacancy is enriched at interfacial sites between Ni and CeO_2.[13,22]

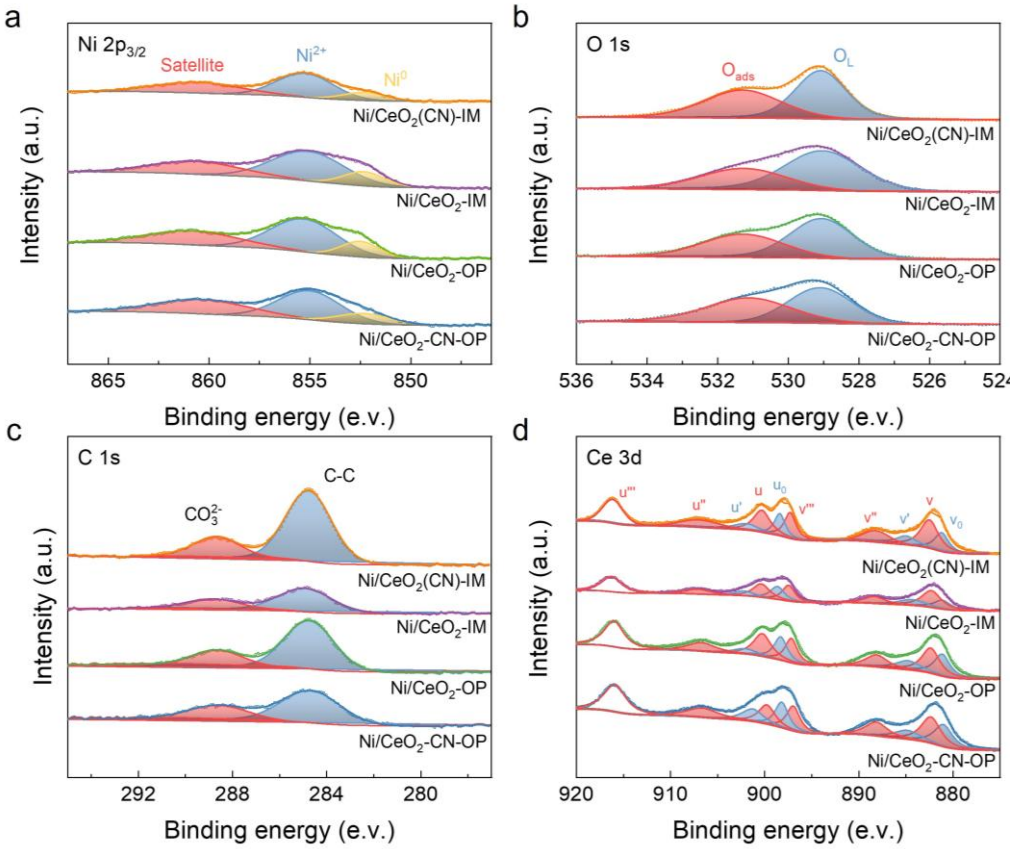

Figure 4. XPS spectra of the Ni/CeO_2 catalysts: (a) Ni 2p3/2, (b) O 1s, (c) C 1s, (d) Ce 3d.

What factors lead to the difference in oxygen vacancy concentration over those prepared catalysts? From the HRTEM of the prepared catalysts (Figure 1e-1h), more CeO_2 (110) facets could be observed over the surface of Ni/CeO_2-CN-OP compared with the other three catalysts. According to the literature, the oxygen vacancy formation energies are 2.28, 1.49, and 1.18 eV over the CeO_2 (111), (100), and (110) facet, respectively.[48] It is reasonable that Ni/CeO_2-CN-OP with more CeO_2 (110) facet possesses higher amount of oxygen vacancy. However, HRTEM represents only a small part of the sample, it could not be used to quantify the different facets of the support. In order to distinguish surface Ce species among CeO_2 facets and obtain their concentrations, ^{31}P MAS NMR test after adsorption of trimethylphosphine was performed (TMP-^{31}P NMR).[49] TMP-^{31}P NMR is only applicable for pure CeO_2 support, thus we just conduct it for CeO_2 and CeO_2(CN) support. Farahnaz et al. reported that ^{31}P chemical shift (δ^{31}P) is -46 ppm on CeO_2 (110) facet obtained by DFT

calculations.[50] In Figure 5a, a $\delta^{31}P$ signal of -44.8 ppm, closer to -46 ppm, can be observed for the CeO_2(CN) support, indicating that the CeO_2(CN) support predominantly exposes (110) facets. The $\delta^{31}P$ depends on the surface electron density. Higher electron density could lead to a weaker interaction of TMP-Ce adducts and more negative $\delta^{31}P$.[51] The surface Ce has higher electron density on (100) facet than that on (110) facet.[52] Therefore, more negative $\delta^{31}P$ for the CeO_2 support (-51.9 ppm) compared with the CeO_2(CN) support (-44.8 ppm) should point to the more (100) facet on the CeO_2 support. The degree of electron sharing between the P atom of TMP and the surface Ce cation determines the electron density of ^{31}P nuclei and hence its magnetic susceptibility under ^{31}P NMR. This implies that the adsorption energy (E_{ad}) of TMP on CeO_2 facets should have a linear relationship with δ ^{31}P. The E_{ad} of free TMP and the E_{ad} of TMP on two CeO_2 facets are 0 eV, -0.81 eV for (110) facet, and -0.38 for (100) facet,[49] exhibiting a linear relationship (R^2 = 0.974) with δ ^{31}P of the corresponding facet (Figure 5b). This confirms the correspondence of δ ^{31}P (-51.9 ppm) and CeO_2 (100) facet.

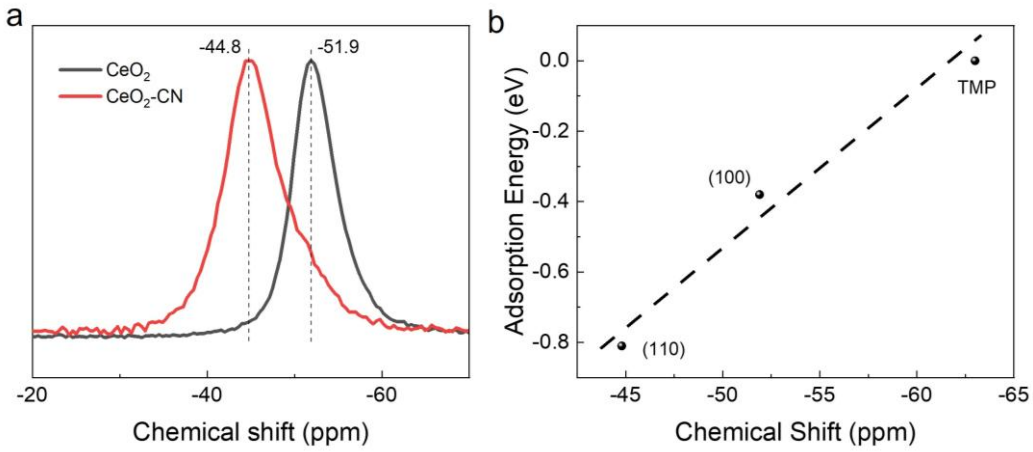

Figure 5. (a) TMP-^{31}P NMR spectra of CeO_2 and CeO_2(CN); (b) Linear regression plot using experimental δ ^{31}P and calculated E_{ad} of CeO_2 facets. Note that δ ^{31}P for a pure TMP molecule is -63 ppm (i.e., adsorption energy = 0 eV).

Based on the Raman, XPS, and TMP-^{31}P NMR test, the addition of carbon nitride during the preparation process could lead to the major exposure of CeO_2 (110) facet with the lower oxygen vacancy formation energies, thus leading to the higher

concentration of oxygen vacancies. Overall, the effects of g-C_3N_4 addition are clear, but the mechanisms leading to these changes in the CeO_2 structure remain hypothetical. We suggest this is mostly related to the impact on CeO_2 crystallites (more anisotropic and showing more of the (110) facet), which may be related to the mildly basic feature of carbon nitride. When added to the aqueous precursor it may locally raise the pH at the Ce-containing interface. That can accelerate the hydrolysis and condensation of Ce species, producing faster nucleation/growth and leading to more anisotropic crystallites. Under these kinetically dominated conditions, higher-energy surfaces such as CeO_2(110) can be preferentially exposed. A more physical blocking/templating effect of g-C_3N_4 on the growth of CeO_2 and the resulting morphology.

3.4. Catalytic Performance. The CO_2 methanation performance was evaluated over Ni/CeO_2 catalysts in the temperature range between 200 and 325 °C with the GHSV of 36000 mL g^{-1} h^{-1}, and the results are shown in Figure 6a. In terms of CH_4 selectivity, all catalysts attain almost 100 % at reaction temperature below 275°C. At higher temperature, Ni/CeO_2-CN-OP, Ni/CeO_2-OP and Ni/CeO_2(CN)-IM catalyst still maintain the CH_4 selectivity above 99 %, whereas a little byproduct CO is generated over Ni/CeO_2-IM catalyst via the reverse water gas shift (RWGS) reaction, resulting in 97 % CH_4 selectivity. In terms of CO_2 conversion, the activity of Ni/CeO_2-CN-OP is higher than that of the other three catalysts at the whole testing temperature range. Especially, at 250 °C, the CO_2 conversion for Ni/CeO_2-CN-OP achieves 82.6%. A comparison of catalytic activity over recently reported catalysts is presented in Table S4. Importantly, the catalytic activity of Ni/CeO_2-CN-OP at low temperature (250 °C) is comparable to the state-of-the-art methanation catalysts in the previous report. Generally, the TOF value is calculated to appraise the intrinsic activity of catalysts. As shown in Table S1, the TOF value of CO_2 conversion over Ni/CeO_2-CN-OP at 225 °C is up to 0.047 s^{-1}, which is 1.24 times, 1.52 times and 1.42 times higher than those over Ni/CeO_2-OP (0.038 s^{-1}), Ni/CeO_2-IM (0.031 s^{-1}), and Ni/CeO_2(CN)-IM (0.033 s^{-1})

respectively. The fact that Ni/CeO_2-CN-OP stand out in terms of TOF, as compared to the other catalysts in the series suggests that Ni dispersion alone is not the main factor that explains the high activity of this catalyst (as discussed below). The stability of Ni/CeO_2-CN-OP was also tested with the GHSV of 36000 mL g^{-1} h^{-1} at 250 °C for 72 h, as shown in Figure 6b. Ni/CeO_2-CN-OP could maintain CO_2 conversion and selectivity above 80% and 99%, respectively.

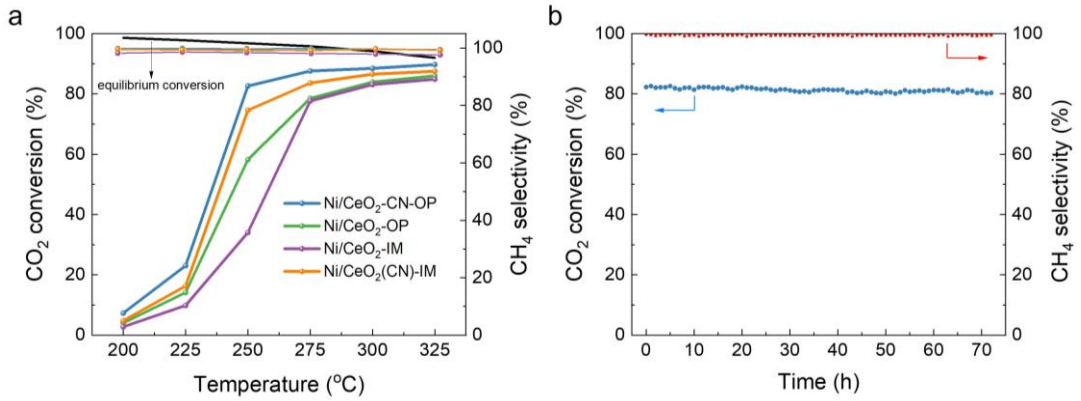

Figure 6. (a) CO_2 methanation performance in terms of CO_2 conversion and CH_4 selectivity as a function of temperature. (b) CO_2 conversion at 250 °C against time on stream over Ni/CeO_2-CN-OP.

3.5. Mechanistic aspects of methanation and impact of C_3N_4

In general, the proposed CO_2 methanation mechanism can be categorized into RWGS+CO hydrogenation pathway and formate pathway. The former pathway involves the dissociation of CO_2 to CO and the hydrogenation of formed CO to CH_4. The latter pathway involves the stepwise hydrogenation of adsorbed CO_2 species into CH_4 without creating any CO species. Here, in-situ DRIFTS were performed under reaction conditions to provide information on the surface intermediates and reaction mechanism. The DRIFTS spectra with the introduction of CO_2 and H_2 on Ni/CeO_2-CN-OP and Ni/CeO_2-IM as a function of temperature are shown in Figure 7a and 7b. For Ni/CeO_2-CN-OP (Figure 7a), as the reaction begins at 50 °C, appreciable peaks assigned to bicarbonate (1477, 1283 cm^{-1}), monodentate carbonate (1587 cm^{-1}), and bidentate carbonate (1402 cm^{-1}) are observed. The peaks of bicarbonate decrease gradually as the temperature increases and can be removed completely below 200 °C.

With the further increase of temperature, the peaks ascribed to monodentate carbonate and bidentate carbonate vanish in succession below 300 °C, accompanied with the growth of some new peaks attributed to monodentate formate (1562 cm^{-1}, 1348 cm^{-1}) and bidentate formate (1518 cm^{-1}, 1379 cm^{-1}). It has been reported that monodentate formate and bidentate formate can be derived from the hydrogenation of monodentate carbonate and bidentate carbonate, respectively.[14] In addition to the carbonate and formate species, the peaks for linear CO (1992 cm^{-1}) and bridged CO (1909 cm^{-1}) species can be clearly seen since 200 °C and 275 °C, separately. CH_4 signal (3015, 1306 cm^{-1}) appears from 225 °C and increases with temperature. Resembling Ni/CeO_2-CN-OP, carbonate and formate species are observed on Ni/CeO_2-IM (Figure 7b) and their evolution has no obvious difference compared with Ni/CeO_2-CN-OP. However, linear CO on Ni/CeO_2-IM appears at higher temperature (250 °C) than that on Ni/CeO_2-CN-OP (200 °C).

Moreover, in-situ DRIFTS experiments were also carried out by switching off the reaction gas 13.3% CO_2/53.2% H_2/He after 30 min exposure at 300 °C and subsequently introducing the gas of 61.5% H_2/He (Figure 7c and 7d). For both Ni/CeO_2-CN-OP and Ni/CeO_2-IM catalysts, the CO peaks disappear immediately (3 min) once upon switching off CO_2. After the depletion of the adsorbed CO, monodentate formate species continuously decreased. Meanwhile, the intensity of CH_4 peak decreases gradually. Consequently, it can be concluded that CO and monodentate formate species over the Ni/CeO_2 catalysts are both the active species in this methanation reaction, with the former is more active and the main contributors to the low temperature methanation performance. It has been reported that oxygen vacancy is crucial for the CO_2 dissociation.[32] To confirm the roles of oxygen vacancy in CO_2 methanation, the relationship between the oxygen vacancy (estimated from the I_D/I_{2g} ratio in Raman results) and the CO_2 conversion is described. As shown in Figure S6, an acceptable correlation between these two parameters is observed at 200 and 225 °C (higher testing temperature is excluded due to the corresponding CO_2 conversion reaching the

equilibrium). It should be noted that the determination coefficient (R^2) is 0.98 at 200 °C, but it decreases to 0.95 upon increasing the temperature to 225 °C, which is due to the proportion of CH_4 formed from RWGS+CO hydrogenation pathway decreases at higher temperature. Thus, it indicates that oxygen vacancy indeed plays a vital role in the methanation reaction, especially at low temperatures.

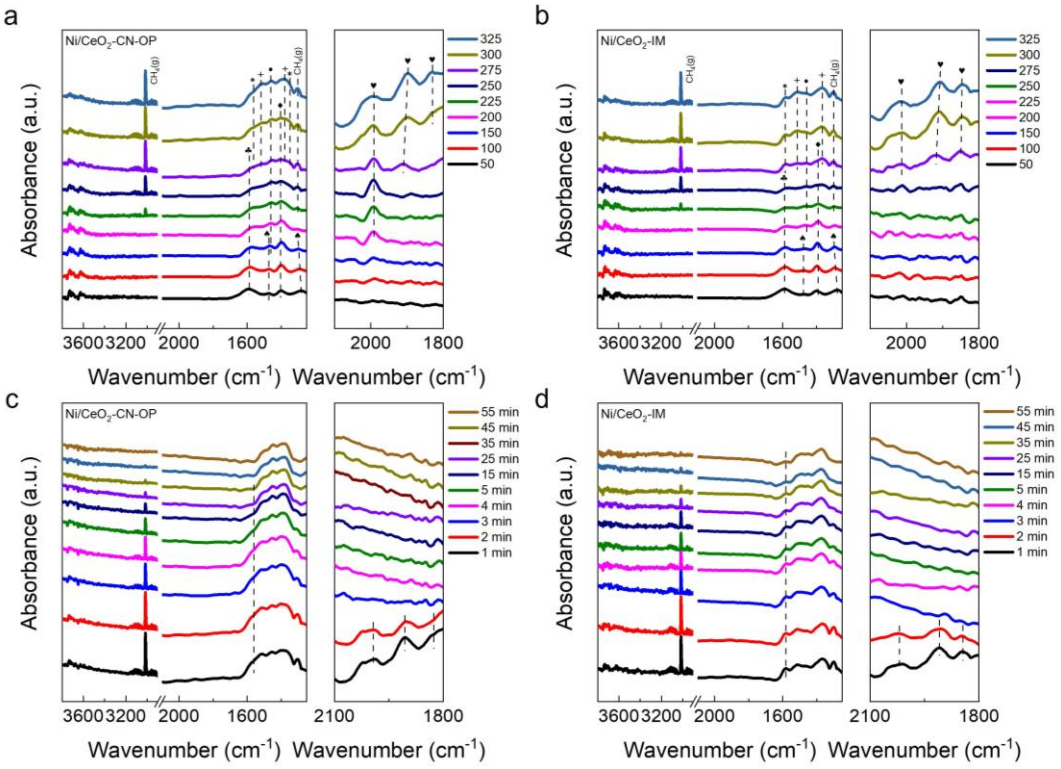

Figure 7. In-situ DRIFTS results of CO_2 hydrogenation on (a) Ni/CeO_2-CN-OP and (b) Ni/CeO_2-IM catalyst; In-situ DRIFTS results of (c) Ni/CeO_2-CN-OP and (d) Ni/CeO_2-IM catalyst at 300 °C under continuous flow of gas 61.5% H_2/He after maintaining at 300 °C for 30 min under reaction gas (13.3% CO_2/53.2% H_2/He). Symbol definition: bicarbonate (♠), monodentate carbonate (♠), bidentate carbonate (◆), monodentate formate (*), bidentate formate (+), carbonyl (♥).

Furthermore, the evolution of monodentate formate on Ni/CeO_2-IM is slower than that on Ni/CeO_2-CN-OP, as observed from Figure 7c and 7d. This difference is due to the less efficient H_2 dissociation on Ni/CeO_2-IM, which may not be sufficient for hydrogenation of the formed monodentate formate species. The amount of chemisorbed H_2 is also calculated for Ni/CeO_2-CN-OP and Ni/CeO_2-IM. Ni/CeO_2-CN-OP shows a

higher amount of chemisorbed H_2 (146 μmol/g_{cat}) than Ni/CeO_2-IM (94 μmol/g_{cat}), thus generating more dissociated hydrogen and further improving hydrogenation activity.

Based on these findings, the RWGS+CO hydrogenation pathway and the formate pathway occurring in parallel over the Ni/CeO_2 catalysts can be identified (Scheme 1). CO_2 is adsorbed by the medium basic site over catalyst surface with the formation of monodentate carbonate, which can be hydrogenated to monodentate formate and then reacts with H atom until CH_4 is formed. In parallel, direct dissociation of CO_2 can be facilitated by surface oxygen vacancies, and the generated CO is further hydrogenated to CH_4. Ni/CeO_2-CN-OP possesses a large amount of oxygen vacancies and medium basic sites, which results in its higher catalytic performance.

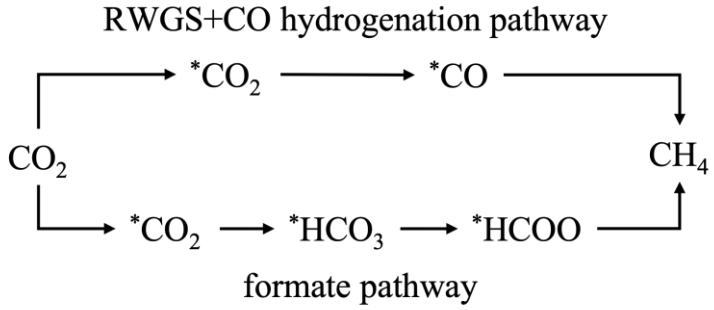

Scheme 1. Proposed reaction pathways of CO_2 methanation over Ni/CeO_2 catalyst.

4. CONCLUSION

In this work, a highly active Ni/CeO_2 was synthesized via a one-pot method promoted with the addition of C_3N_4. The catalyst demonstrated exceptional performance, achieving a high CO_2 conversion (82.6%) and CH_4 selectivity (99.4%), corresponding to a CH_4 production rate of 178 mmol g_{cat}^{-1} h^{-1} at 250 °C. Notably, this specific methane productivity represents the highest reported for Ni-CeO_2 catalysts at 250 °C. Furthermore, this catalytic activity was fully maintained during a 72-h on-stream test. Mechanistic investigations confirmed that both the RWGS+CO hydrogenation pathway and formate pathway contribute to CO_2 methanation, with the former dominating at low temperatures. The one-pot synthesis approach and C_3N_4 addition were found to enhance the concentration of oxygen vacancies and the density of surface medium-strength basic

sites, thereby promoting CO_2 activation and the formation of monodentate carbonate species. As a result, both reaction pathways were significantly accelerated, contributing to the catalyst's superior methanation performance.

ACKNOWLEDGMENT

YZ thanks the Chinese Scholarship Council (CSC)for his PhD fellowship. DPD thanks the Francqui Foundation for the Francqui Research Professor chair.

REFERENCE

(1) Karelovic, A.; Ruiz, P. Improving the Hydrogenation Function of Pd/γ-Al_2O_3 Catalyst by Rh/γ-Al_2O_3 Addition in CO_2 Methanation at Low Temperature. *ACS Catal.* **2013**, *3* (12), 2799–2812. https://doi.org/10.1021/cs400576w.

(2) Hasan, M. M. F.; Rossi, L. M.; Debecker, D. P.; Leonard, K. C.; Li, Z.; Makhubela, B. C. E.; Zhao, C.; Kleij, A. Can CO_2 and Renewable Carbon Be Primary Resources for Sustainable Fuels and Chemicals? *ACS Sustain. Chem. Eng.* **2021**, *9* (37), 12427–12430. https://doi.org/10.1021/acssuschemeng.1c06008.

(3) Molinet-Chinaglia, C.; Shafiq, S.; Serp, P. Low Temperature Sabatier CO_2 Methanation. *ChemCatChem* **2024**, *16* (24), e202401213. https://doi.org/10.1002/cctc.202401213.

(4) Xu, D.; Wang, Y.; Ding, M.; Hong, X.; Liu, G.; Tsang, S. C. E. Advances in Higher Alcohol Synthesis from CO_2 Hydrogenation. *Chem* **2021**, *7* (4), 849–881. https://doi.org/10.1016/j.chempr.2020.10.019.

(5) Shen, L.; Xu, J.; Zhu, M.; Han, Y.-F. Essential Role of the Support for Nickel-Based CO_2 Methanation Catalysts. *ACS Catal.* **2020**, *10* (24), 14581–14591. https://doi.org/10.1021/acscatal.0c03471.

(6) Li, Z.-X.; Fu, X.-P.; Ma, C.; Wang, W.-W.; Liu, J.-C.; Jia, C.-J. Identifying the Key Structural Features of Ni-Based Catalysts for the CO_2 Methanation Reaction. *J. Catal.* **2024**, *436*, 115585. https://doi.org/10.1016/j.jcat.2024.115585.

(7) Cárdenas-Arenas, A.; Quindimil, A.; Davó-Quiñonero, A.; Bailón-García, E.; Lozano-Castelló, D.; De-La-Torre, U.; Pereda-Ayo, B.; González-Marcos, J. A.; González-Velasco, J. R.; Bueno-López, A. Isotopic and in Situ DRIFTS Study of the CO_2 Methanation Mechanism Using Ni/CeO_2 and Ni/Al_2O_3 Catalysts. *Appl. Catal. B Environ.* **2020**, *265*, 118538. https://doi.org/10.1016/j.apcatb.2019.118538.

(8) Cerdá-Moreno, C.; Chica, A.; Keller, S.; Rautenberg, C.; Bentrup, U. Ni-Sepiolite and Ni-Todorokite as Efficient CO_2 Methanation Catalysts: Mechanistic Insight by

Operando DRIFTS. *Appl. Catal. B Environ.* **2020**, *264*, 118546. https://doi.org/10.1016/j.apcatb.2019.118546.
(9) Jia, X.; Zhang, X.; Rui, N.; Hu, X.; Liu, C. Structural Effect of Ni/ZrO_2 Catalyst on CO_2 Methanation with Enhanced Activity. *Appl. Catal. B Environ.* **2019**, *244*, 159–169. https://doi.org/10.1016/j.apcatb.2018.11.024.
(10) Xu, X.; Liu, L.; Tong, Y.; Fang, X.; Xu, J.; Jiang, D.; Wang, X. Facile Cr^{3+}-Doping Strategy Dramatically Promoting Ru/CeO_2 for Low-Temperature CO_2 Methanation: Unraveling the Roles of Surface Oxygen Vacancies and Hydroxyl Groups. *ACS Catal.* **2021**, *11* (9), 5762–5775. https://doi.org/10.1021/acscatal.0c05468.
(11) Xie, Y.; Chen, J.; Wu, X.; Wen, J.; Zhao, R.; Li, Z.; Tian, G.; Zhang, Q.; Ning, P.; Hao, J. Frustrated Lewis Pairs Boosting Low-Temperature CO_2 Methanation Performance over Ni/CeO_2 Nanocatalysts. *ACS Catal.* **2022**, *12* (17), 10587–10602. https://doi.org/10.1021/acscatal.2c02535.
(12) Zhao, Y.; Girelli, V.; Ersen, O.; Debecker, D. P. CO_2 Methanation with High-Loading Mesoporous Ni/SiO_2 Catalysts: Toward High Specific Activity and New Mechanistic Insights. *J. Catal.* **2023**, *426*, 283–293. https://doi.org/10.1016/j.jcat.2023.07.021.
(13) Hongmanorom, P.; Ashok, J.; Chirawatkul, P.; Kawi, S. Interfacial Synergistic Catalysis over Ni Nanoparticles Encapsulated in Mesoporous Ceria for CO_2 Methanation. *Appl. Catal. B Environ.* **2021**, *297*, 120454. https://doi.org/10.1016/j.apcatb.2021.120454.
(14) Pan, Q.; Peng, J.; Sun, T.; Wang, S.; Wang, S. Insight into the Reaction Route of CO_2 Methanation: Promotion Effect of Medium Basic Sites. *Catal. Commun.* **2014**, *45*, 74–78. https://doi.org/10.1016/j.catcom.2013.10.034.
(15) Vrijburg, W. L.; Moioli, E.; Chen, W.; Zhang, M.; Terlingen, B. J. P.; Zijlstra, B.; Filot, I. A. W.; Züttel, A.; Pidko, E. A.; Hensen, E. J. M. Efficient Base-Metal NiMn/TiO_2 Catalyst for CO_2 Methanation. *ACS Catal.* **2019**, *9* (9), 7823–7839. https://doi.org/10.1021/acscatal.9b01968.
(16) Guo, Y.; Mei, S.; Yuan, K.; Wang, D.-J.; Liu, H.-C.; Yan, C.-H.; Zhang, Y.-W. Low-Temperature CO_2 Methanation over CeO_2-Supported Ru Single Atoms, Nanoclusters, and Nanoparticles Competitively Tuned by Strong Metal–Support Interactions and H-Spillover Effect. *ACS Catal.* **2018**, *8* (7), 6203–6215. https://doi.org/10.1021/acscatal.7b04469.
(17) Ocampo, F.; Louis, B.; Roger, A.-C. Methanation of Carbon Dioxide over Nickel-Based $Ce_{0.72}Zr_{0.28}O_2$ Mixed Oxide Catalysts Prepared by Sol–Gel Method. *Appl. Catal. Gen.* **2009**, *369* (1–2), 90–96. https://doi.org/10.1016/j.apcata.2009.09.005.
(18) Ashok, J.; Ang, M. L.; Kawi, S. Enhanced Activity of CO2 Methanation over Ni/CeO2-ZrO2 Catalysts: Influence of Preparation Methods. *Catal. Today* **2017**, *281*, 304–311. https://doi.org/10.1016/j.cattod.2016.07.020.
(19) Wang, F.; He, S.; Chen, H.; Wang, B.; Zheng, L.; Wei, M.; Evans, D. G.; Duan, X. Active Site Dependent Reaction Mechanism over Ru/CeO_2 Catalyst toward CO_2

Methanation. *J. Am. Chem. Soc.* **2016**, *138* (19), 6298–6305. https://doi.org/10.1021/jacs.6b02762.
(20) Chen, S.; Costley-Wood, L.; Lezcano-Gonzalez, I.; Campbell, E.; Weng, Z.; Asunción Molina, M.; Wu, Y.; Beale, A. M. Understanding Defect Generation on CeO_2 and Its Utilization for Enhanced Metal-Support Interactions in Ni/CeO_2 Catalysts for Improved CO_2 Methanation Performance. *Appl. Catal. B Environ. Energy* **2025**, *366*, 125029. https://doi.org/10.1016/j.apcatb.2025.125029.
(21) Liu, Y.; Li, D.; Zhao, H.; Wang, C.; Xu, Y.; Li, L.; Li, Z.; Wang, H.; Li, K. Boosting CO_2 Methanation Activity by Tuning Ni Crystal Plane and Oxygen Vacancy in Ni/CeO_2 Catalyst. *Chem. Eng. J.* **2024**, *494*, 153004. https://doi.org/10.1016/j.cej.2024.153004.
(22) Rui, N.; Zhang, X.; Zhang, F.; Liu, Z.; Cao, X.; Xie, Z.; Zou, R.; Senanayake, S. D.; Yang, Y.; Rodriguez, J. A.; Liu, C.-J. Highly Active Ni/CeO_2 Catalyst for CO_2 Methanation: Preparation and Characterization. *Appl. Catal. B Environ.* **2021**, *282*, 119581. https://doi.org/10.1016/j.apcatb.2020.119581.
(23) Ye, R.-P.; Li, Q.; Gong, W.; Wang, T.; Razink, J. J.; Lin, L.; Qin, Y.-Y.; Zhou, Z.; Adidharma, H.; Tang, J.; Russell, A. G.; Fan, M.; Yao, Y.-G. High-Performance of Nanostructured Ni/CeO_2 Catalyst on CO_2 Methanation. *Appl. Catal. B Environ.* **2020**, *268*, 118474. https://doi.org/10.1016/j.apcatb.2019.118474.
(24) Zhang, S.; Feng, H.; Li, C.; Cao, X.; Li, H.; Wu, Y. The Reduction Mechanism of C1 Product from Carbon Dioxide Catalyzed by Ni-Doped g-C_3N_4. *Mol. Catal.* **2024**, *559*, 114064. https://doi.org/10.1016/j.mcat.2024.114064.
(25) Singh, R.; Wang, L.; Sun, H.; Huang, J. CO_2 Hydrogenation Using Size-Dependent Ru Particles Supported on g-C_3N_4. *Carbon Capture Sci. Technol.* **2024**, *13*, 100248. https://doi.org/10.1016/j.ccst.2024.100248.
(26) Ma, L.; Guan, R.; Kang, W.; Sun, Z.; Li, H.; Li, Q.; Shen, Q.; Chen, C.; Liu, X.; Jia, H.; Xue, J. Preparation of Highly Dispersed Ni Single-Atom Doped Ultrathin g-C3N4 Nanosheets by Metal Vapor Exfoliation for Efficient Photocatalytic CO_2 Reduction. *J. Colloid Interface Sci.* **2024**, *660*, 381–392. https://doi.org/10.1016/j.jcis.2024.01.023.
(27) Yang, P.; Shang, L.; Zhao, J.; Zhang, M.; Shi, H.; Zhang, H.; Yang, H. Selectively Constructing Nitrogen Vacancy in Carbon Nitrides for Efficient Syngas Production with Visible Light. *Appl. Catal. B Environ.* **2021**, *297*, 120496. https://doi.org/10.1016/j.apcatb.2021.120496.
(28) Liu, W.; Li, L.; Lin, S.; Luo, Y.; Bao, Z.; Mao, Y.; Li, K.; Wu, D.; Peng, H. Confined Ni-In Intermetallic Alloy Nanocatalyst with Excellent Coking Resistance for Methane Dry Reforming. *J. Energy Chem.* **2022**, *65*, 34–47. https://doi.org/10.1016/j.jechem.2021.05.017.
(29) Liu, K.; Zakharova, N.; Adeyilola, A.; Zeng, L. Experimental Study on the Pore Shape Damage of Shale Samples during the Crushing Process. *Energy Fuels* **2021**, *35* (3), 2183–2191. https://doi.org/10.1021/acs.energyfuels.0c03297.

(30) Li, Y.; Men, Y.; Liu, S.; Wang, J.; Wang, K.; Tang, Y.; An, W.; Pan, X.; Li, L. Remarkably Efficient and Stable Ni/Y_2O_3 Catalysts for CO_2 Methanation: Effect of Citric Acid Addition. *Appl. Catal. B Environ.* **2021**, *293*, 120206. https://doi.org/10.1016/j.apcatb.2021.120206.

(31) Li, J.; Zhou, Y.; Xiao, X.; Wang, W.; Wang, N.; Qian, W.; Chu, W. Regulation of Ni–CNT Interaction on Mn-Promoted Nickel Nanocatalysts Supported on Oxygenated CNTs for CO_2 Selective Hydrogenation. *ACS Appl. Mater. Interfaces* **2018**, *10* (48), 41224–41236. https://doi.org/10.1021/acsami.8b04220.

(32) Zhang, T.; Wang, W.; Gu, F.; Xu, W.; Zhang, J.; Li, Z.; Zhu, T.; Xu, G.; Zhong, Z.; Su, F. Enhancing the Low-Temperature CO2 Methanation over Ni/La-CeO_2 Catalyst: The Effects of Surface Oxygen Vacancy and Basic Site on the Catalytic Performance. *Appl. Catal. B Environ.* **2022**, *312*, 121385. https://doi.org/10.1016/j.apcatb.2022.121385.

(33) Tada, S.; Nagase, H.; Fujiwara, N.; Kikuchi, R. What Are the Best Active Sites for CO_2 Methanation over Ni/CeO_2? *Energy Fuels* **2021**, *35* (6), 5241–5251. https://doi.org/10.1021/acs.energyfuels.0c04238.

(34) Si, R.; Flytzani-Stephanopoulos, M. Shape and Crystal-Plane Effects of Nanoscale Ceria on the Activity of Au-CeO_2 Catalysts for the Water–Gas Shift Reaction. *Angew. Chem. Int. Ed.* **2008**, *47* (15), 2884–2887. https://doi.org/10.1002/anie.200705828.

(35) Saw, E. T.; Oemar, U.; Ang, M. L.; Kus, H.; Kawi, S. High-Temperature Water Gas Shift Reaction on Ni–Cu/CeO_2 Catalysts: Effect of Ceria Nanocrystal Size on Carboxylate Formation. *Catal. Sci. Technol.* **2016**, *6* (14), 5336–5349. https://doi.org/10.1039/C5CY01932J.

(36) Saw, E. T.; Oemar, U.; Tan, X. R.; Du, Y.; Borgna, A.; Hidajat, K.; Kawi, S. Bimetallic Ni–Cu Catalyst Supported on CeO_2 for High-Temperature Water–Gas Shift Reaction: Methane Suppression via Enhanced CO Adsorption. *J. Catal.* **2014**, *314*, 32–46. https://doi.org/10.1016/j.jcat.2014.03.015.

(37) Muroyama, H.; Tsuda, Y.; Asakoshi, T.; Masitah, H.; Okanishi, T.; Matsui, T.; Eguchi, K. Carbon Dioxide Methanation over Ni Catalysts Supported on Various Metal Oxides. *J. Catal.* **2016**, *343*, 178–184. https://doi.org/10.1016/j.jcat.2016.07.018.

(38) Italiano, C.; Llorca, J.; Pino, L.; Ferraro, M.; Antonucci, V.; Vita, A. CO and CO_2 Methanation over Ni Catalysts Supported on CeO_2, Al_2O_3 and Y_2O_3 Oxides. *Appl. Catal. B Environ.* **2020**, *264*, 118494. https://doi.org/10.1016/j.apcatb.2019.118494.

(39) Xu, X.; Tong, Y.; Huang, J.; Zhu, J.; Fang, X.; Xu, J.; Wang, X. Insights into CO_2 Methanation Mechanism on Cubic ZrO_2 Supported Ni Catalyst via a Combination of Experiments and DFT Calculations. *Fuel* **2021**, *283*, 118867. https://doi.org/10.1016/j.fuel.2020.118867.

(40) Ni, J.; Chen, L.; Lin, J.; Kawi, S. Carbon Deposition on Borated Alumina Supported Nano-Sized Ni Catalysts for Dry Reforming of CH4. *Nano Energy* **2012**, *1* (5), 674–686. https://doi.org/10.1016/j.nanoen.2012.07.011.

(41) Németh, M.; Srankó, D.; Károlyi, J.; Somodi, F.; Schay, Z.; Sáfrán, G.; Sajó, I.; Horváth, A. Na-Promoted Ni/ZrO_2 Dry Reforming Catalyst with High Efficiency: Details of Na_2O-ZrO_2-Ni Interaction Controlling Activity and Coke Formation. *Catal. Sci. Technol.* **2017**, *7* (22), 5386–5401. https://doi.org/10.1039/C7CY01011G.

(42) Fan, L.; Zhang, J.; Ma, K.; Zhang, Y.; Hu, Y.-M.; Kong, L.; Jia, A.; Zhang, Z.; Huang, W.; Lu, J.-Q. Ceria Morphology-Dependent Pd-CeO2 Interaction and Catalysis in CO_2 Hydrogenation into Formate. *J. Catal.* **2021**, *397*, 116–127. https://doi.org/10.1016/j.jcat.2021.03.025.

(43) Löfberg, A.; Guerrero-Caballero, J.; Kane, T.; Rubbens, A.; Jalowiecki-Duhamel, L. Ni/CeO_2 Based Catalysts as Oxygen Vectors for the Chemical Looping Dry Reforming of Methane for Syngas Production. *Appl. Catal. B Environ.* **2017**, *212*, 159–174. https://doi.org/10.1016/j.apcatb.2017.04.048.

(44) Pan, Q.; Peng, J.; Sun, T.; Gao, D.; Wang, S.; Wang, S. CO_2 Methanation on Ni/$Ce_{0.5}Zr_{0.5}O_2$ Catalysts for the Production of Synthetic Natural Gas. *Fuel Process. Technol.* **2014**, *123*, 166–171. https://doi.org/10.1016/j.fuproc.2014.01.004.

(45) Idriss, H. On the Wrong Assignment of the XPS O1s Signal at 531–532 eV Attributed to Oxygen Vacancies in Photo- and Electro-Catalysts for Water Splitting and Other Materials Applications. *Surf. Sci.* **2021**, *712*, 121894. https://doi.org/10.1016/j.susc.2021.121894.

(46) Wang, J.; Mueller, D. N.; Crumlin, E. J. Recommended Strategies for Quantifying Oxygen Vacancies with X-Ray Photoelectron Spectroscopy. *J. Eur. Ceram. Soc.* **2024**, *44* (15), 116709. https://doi.org/10.1016/j.jeurceramsoc.2024.116709.

(47) Tang, Y.; Wei, Y.; Wang, Z.; Zhang, S.; Li, Y.; Nguyen, L.; Li, Y.; Zhou, Y.; Shen, W.; Tao, F. F.; Hu, P. Synergy of Single-Atom Ni_1 and Ru_1 Sites on CeO_2 for Dry Reforming of CH_4. *J. Am. Chem. Soc.* **2019**, *141* (18), 7283–7293. https://doi.org/10.1021/jacs.8b10910.

(48) Zhang, W.; Pu, M.; Lei, M. Theoretical Studies on the Stability and Reactivity of the Metal-Doped CeO_2 (100) Surface: Toward H_2 Dissociation and Oxygen Vacancy Formation. *Langmuir* **2020**, *36* (21), 5891–5901. https://doi.org/10.1021/acs.langmuir.0c00644.

(49) Tan, Z.; Li, G.; Chou, H.-L.; Li, Y.; Yi, X.; Mahadi, A. H.; Zheng, A.; Edman Tsang, S. C.; Peng, Y.-K. Differentiating Surface Ce Species among CeO_2 Facets by Solid-State NMR for Catalytic Correlation. *ACS Catal.* **2020**, *10* (7), 4003–4011. https://doi.org/10.1021/acscatal.0c00014.

(50) Maleki, F.; Pacchioni, G. Probing the Nature of Lewis Acid Sites on Oxide Surfaces with $^{31}P(CH_3)_3$ NMR: A Theoretical Analysis. *Phys. Chem. Chem. Phys.* **2022**, *24* (33), 19773–19782. https://doi.org/10.1039/D2CP03306B.

(51) Peng, Y.-K.; Ye, L.; Qu, J.; Zhang, L.; Fu, Y.; Teixeira, I. F.; McPherson, I. J.; He, H.; Tsang, S. C. E. Trimethylphosphine-Assisted Surface Fingerprinting of Metal Oxide Nanoparticle by ^{31}P Solid-State NMR: A Zinc Oxide Case Study. *J. Am. Chem. Soc.* **2016**, *138* (7), 2225–2234. https://doi.org/10.1021/jacs.5b12080.
(52) Goris, B.; Turner, S.; Bals, S.; Van Tendeloo, G. Three-Dimensional Valency Mapping in Ceria Nanocrystals. *ACS Nano* **2014**, *8* (10), 10878–10884. https://doi.org/10.1021/nn5047053.